

when γ -rays were first detected from PKS 0346-27 region by Fermi-LAT and the source was included in the Fermi-LAT First Source Catalog (1FGL, [Abdo et al. \(2010a\)](#)). In the latest Fermi-LAT Fourth Source Catalog (4FGL, [Abdollahi et al. \(2020\)](#)), it is associated with the γ -ray source 4FGL J0348.5-2749.

Based on the data taken on 2017 Nov 14 (MJD 58071), a near-infrared (NIR) flare was first reported from PKS 0346-27 ([Carrasco et al. \(2017\)](#)). A few months later, on 2018 Feb 02 (MJD 58151), strong γ -ray flaring activity was reported from the source based on the Fermi-LAT data ([Angioni \(2018\)](#)). PKS 0346-27 was found in an elevated state with a significantly harder spectrum with respect to the one reported in the 3FGL and reaching a daily γ -ray flux (energy > 100 MeV) more than 100 times larger than the average flux reported in the 3FGL. Multiwavelength follow-up observations revealed enhanced activity in the optical-NIR ([Nesci \(2018a\)](#); [Vallely et al. \(2018\)](#)), ultra-violet (UV) and X-ray ([Nesci \(2018b\)](#)). A multi-wavelength broad-band spectral study has been reported by [Angioni et al. \(2019\)](#). They did a comparative study between the quiescent and the flaring states in 2018. They fitted the SEDs with a one-zone leptonic model and found that the gamma-ray emission region has a lower magnetic field and a higher Lorentz factor for the flaring state in comparison to a quiescent state. They also found that the peak position of the low-energy hump shifts as the source goes into a flaring state towards higher energies, meaning the blazar classification mentioned earlier is time-dependent. During the quiescent state, the source would be classified as an LSP, and during the flaring state as an ISP. In our analysis, since we have analyzed the source only when it is in a flaring state, we do not see a change in the position of the low-energy peak. Peak positions for all flares above 10^{14} Hz meaning they would be classified as ISP.

In this work, we have studied the flaring states between 2019 January and 2021 December (MJD 58484-59575) using γ -ray and X-ray/UVOT data. We characterize the flaring activity of PKS 0346-27 for this period, probing the temporal behavior in γ -rays. Multi-wavelength light curves are generated to identify flaring episodes. In section 2, we discuss multiwavelength observations and data analysis techniques for different archival data. The sum-of-exponentials fitting of γ -ray flares is discussed in section 3. In section 5, the broadband spectral energy distributions (SEDs) and their modeling are discussed. The power density spectrum of γ -ray light curve is discussed in section 6 and our results are discussed in section 7.

2 MULTIWAVELENGTH OBSERVATIONS AND DATA ANALYSIS

2.1 Fermi-LAT

Fermi is a space-based gamma-ray telescope launched in June 2008. The Large Area Telescope (LAT) and the Gamma-ray Burst Monitor (GBM) are the two instruments onboard the telescope. With a maximum effective area (1-10 GeV energy range) of 9500 cm^2 at normal incidence, LAT mainly operates in the 20 MeV-300 GeV energy range, although it is sensitive to energies outside this interval. The on-axis energy resolution is 9%-15% for 100 MeV-1 GeV gamma-rays. The multiple interleaved tungsten and silicon layers act as a converter-tracker system. The tungsten layers convert the gamma-rays into electron-positron pairs and the silicon-strip layers record the tracks of these charged particles to estimate the direction of the incident radiation. The energy of an incident gamma-ray is estimated from the energy deposited by the corresponding electron-positron pair on the calorimeter made of Cs(Tl) crystals at the base

of LAT. The instrument has a Field of View (FoV) of 2.4 sr along with an angular resolution of $< 3.5^\circ$ at 100 MeV and $< 0.15^\circ$ at 10 GeV ([Atwood et al. \(2009\)](#)). The cosmic rays are a major contributor to the background noise in the LAT operating energy range. The ratio of charged cosmic rays to gamma-ray detections for the LAT is in the range of $10^3 - 10^5$ ([Ajello et al. \(2021\)](#)). The Anti-Coincidence Detector (ACD) which surrounds the converter-tracker layers is responsible for differentiating between the two radiations.

Observations of the object PKS 0346-27 from MJD 58484 to MJD 59575 were selected for analysis with a 10° circular Region of Interest (ROI) centered at the source. (RA=57.1589, Dec=-27.8204).

The Fermi-LAT data were analyzed using the recommended `fermitools`¹ package. The data in the energy range 100 MeV to 300 GeV was obtained for the period MJD 58484-59575. The photon data was filtered using `gselect` tool with the constraints `evclass=128` and `evtype=3`. The zenith angle for the observations was restricted to less than 90 degrees to avoid contamination from Earth's limb. The time intervals were filtered using the constraint `'(DATA_QUAL > 0)&&(LAT_CONFIG == 1)'` in the `gtmktime` tool. The light curve was binned in 1-day intervals using the `gtbin` tool and the exposure in cm^2s was computed using `gtexposure`. The flux can be obtained from the counts and exposure terms.

Using the event file obtained in the gamma-ray light curve analysis, a live time HealPix table was computed for the region of interest from the `expCube` tool. An exposure map for a radius of 10 degrees more than the ROI was computed using the live time HealPix table and the `expMap` function with the instrument response file `P8R3_SOURCE_V3` as input. A total of 131 point sources and 1 extended source were identified in the region of interest using the user-contributed tool `make4FGLxml.py`². The background files `gll_iem_v07.fits`³ and `iso_P8R3_SOURCE_V3_v1.txt`⁴ were used for the response model. The models and their respective parameters of the nearby sources were stored in an XML file and the diffusion response was computed. The γ -ray light curve shown in the top panel of Figure 1 is obtained with a 24-hour bin size. The gamma-ray spectral analysis is explained in section 4.

2.2 Swift-XRT

The Neil Gehrels Swift observatory was launched in November 2004 aboard the Delta II rocket with three instruments onboard i.e., the Burst Alert Telescope (BAT), the X-Ray Telescope (XRT), and the Ultra-violet Optical Telescope (UVOT). The Swift-XRT is a grazing incidence Wolter-I telescope with an effective area of 110 cm^2 and a 0.2-10 keV energy range.

A total of 30 observations from Swift-XRT (see Table 1) were available in the same time period as the Fermi observations. The exposure times for these observations span from 1100 to 3800 seconds in the period MJD 58508 to MJD 58701. The lack of observations from MJD 58701 for X-ray analysis is a drawback. Software tools from the HEASoft package were used for analysis.

The XRT data was analyzed using `Xselect` and `Xspec` tools available in HEASoft Software. The Level 1 data is passed to `xrtpipeline`

¹ <https://github.com/fermi-lat/Fermitools-conda/>

² <https://fermi.gsfc.nasa.gov/ssc/data/analysis/user/make4FGLxml.py>

³ <https://fermi.gsfc.nasa.gov/ssc/data/access/lat/BackgroundModels.html>

⁴ <https://fermi.gsfc.nasa.gov/ssc/data/access/lat/BackgroundModels.html>

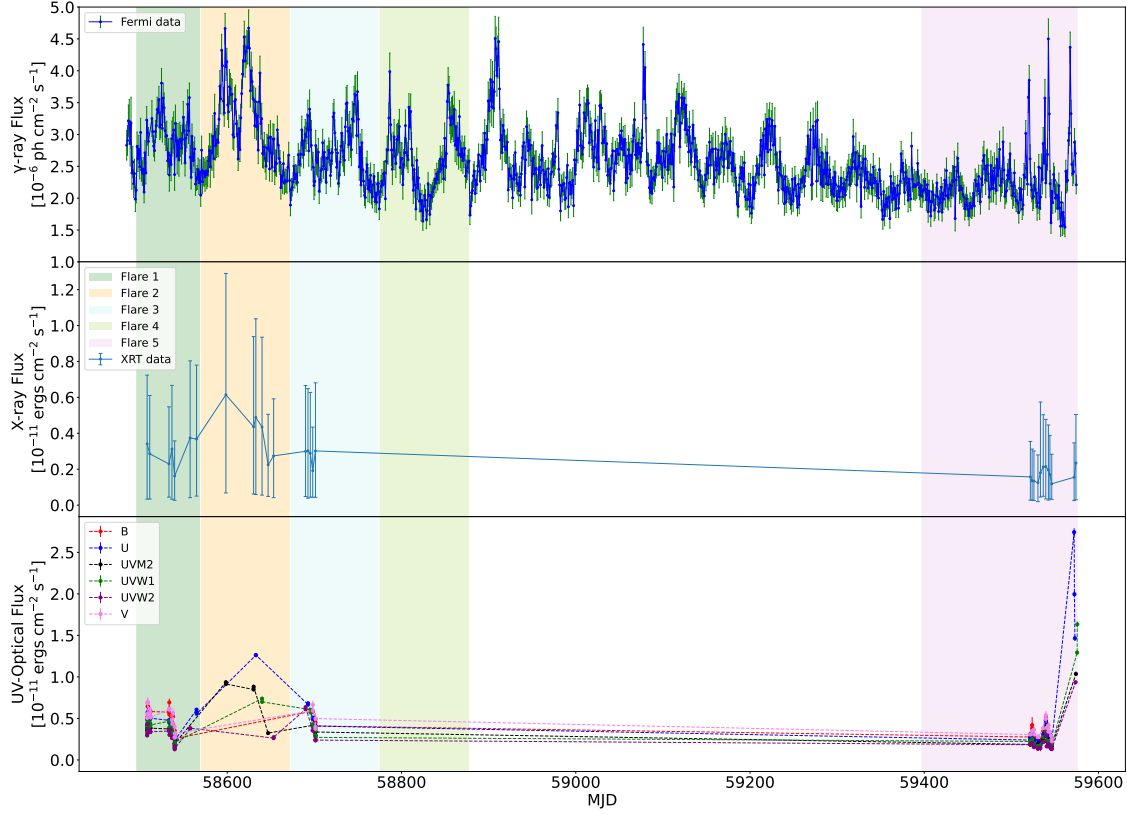


Figure 1. Multi-wavelength light curve of PKS 0346-27 in the period MJD 58484-59575. The time period is further divided into Flares 1-5 for observing changes in spectral parameters over time. (Top panel) One-day binned γ – ray light curve obtained from Fermi-LAT data using aperture photometry method in the 0.1-300 GeV energy range. (Middle panel) X-ray light curve generated from 30 Swift-XRT observations in the energy range 0.3-8 keV. (Bottom panel) Light curves for six Swift-UVOT bands (V, B, U, UVM1, UVM2, and UVW2) were obtained from the same observations as Swift-XRT. Swift data for the period between MJD 58702 and MJD 59520 is not available.

resulting in the generation of Level 2 files used for further analysis. Using the event file and Xselect tools, the image file is extracted which is further used to create source and background regions in the DS9 viewer. The source region file contains a circular 60-arcsec region and the background region file is a circular 120-arcsec region adjacent to the source. Again using Xselect, both the light curves and the spectra were extracted for source and background regions.

The auxiliary response file was generated using the "xrtmkarf" tool, with the image and the source spectrum files generated using "Xselect" as inputs. The "quzcf" tool was used to find the corresponding redistribution matrix file. Using "grppha", the source and background files, the redistribution matrix file, and the auxiliary response file are combined into one spectrum file for Xspec analysis. Xspec was used to model the X-ray spectra with an energy range of 0.3-0.8 KeV. The power law model with $N_H (= 8.16 \times 10^{19} \text{ cm}^{-2})$ was used to model the spectra.

2.3 Swift-UVOT

In the same period as Swift-XRT observations, a total of 166 observations were available for Swift-UVOT analysis with exposure times ranging from 31 to 1626 seconds. The image data files for all observations were combined using the *uvotimsum* tool. Then, the source and background files from the X-ray analysis were used as inputs to the *uvotsource* tool along with the combined image file. The UVOT data is recorded at six wavelengths namely UVW2 (1928 Å), UVM2 (2246 Å), UVM1 (2600 Å), V (3464 Å), U (4392 Å), B (5468 Å). The flux obtained from "uvotsource" is multiplied with the corresponding wavelengths to obtain the energy flux in $\text{erg cm}^{-2} \text{ s}^{-1}$.

3 MULTI-WAVEBAND LIGHT CURVE

3.1 Fitting the light curve

The gamma-ray light curve with 24 hr bins was divided into five flares corresponding to the largest peaks and troughs. The segments

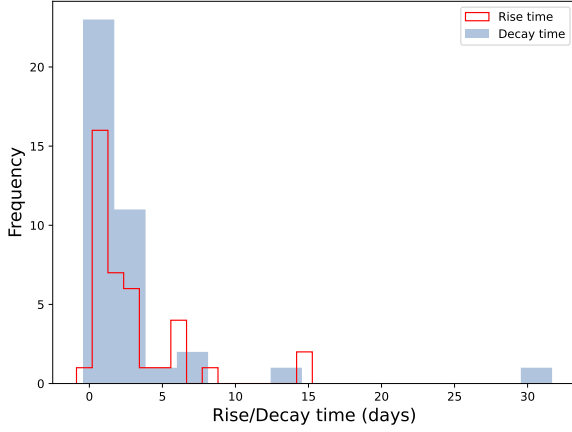


Figure 2. Statistical distribution of Rise (R_t) and Decay (D_t) times of the local peaks identified in the γ – ray light curve show in Figure 3.

Observation ID	MJD	Exposure time (s)
38373017	58508	3502.7
38373018	58511	3768.5
38373019	58533	1526.9
38373020	58537	2630.3
38373021	58540	2576.6
38373022	58557	2998.4
38373023	58565	2601.0
38373024	58598	2877.3
38373026	58630	1969.7
38373027	58633	2009.7
38373028	58640	1983.3
38373029	58647	1108.4
38373030	58653	1947.8
38373031	58690	1988.3
38373032	58693	1835.3
38373033	58695	1785.2
38373034	58698	2020.9
38373035	58701	1898.0
38373036	59522	1978.3
38373037	59524	1842.9
38373040	59526	2203.9
38373043	59530	2146.2
38373044	59533	569.2
38373045	59537	1609.7
38373046	59540	2101.1
38373047	59543	2492.3
38373048	59544	2173.8
38373050	59546	1860.4
38373051	59572	2028.4
38373052	59574	2733.0

Table 1. Swift observations used for this analysis

flare 1, flare 2, flare 3, flare 4, and flare 5 have the time periods MJD 58494–58569, MJD 58570–58672, MJD 58673–58774, MJD 58775–58879, and MJD 59396–59575 respectively. Further, it is observed that individual flares have their own substructure with multiple peaks (see Figure 3). These are modeled using the sum-of-exponentials function given in equation 1.

Instrument	Wavelength	Minimum variability time (days)
Fermi-LAT	Gamma-ray	1.343 ± 0.301
Swift-XRT	X-ray	3.237 ± 2.652
Swift-UVOT	UVW2	0.156 ± 0.068
	UVM2	0.144 ± 0.074
	UVW1	0.105 ± 0.098
	U	0.160 ± 0.185
	B	0.131 ± 0.058
	V	0.102 ± 0.053

Table 2. Minimum variability times from light curves of different wavelengths.

$$A(t) = A_0 + \sum_{i=1}^n 2C_i \left(\exp\left(\frac{P_{ti} - t}{R_{ti}}\right) + \exp\left(\frac{t - P_{ti}}{D_{ti}}\right) \right) \quad (1)$$

where $A(t)$ is the flux magnitude, A_0 is the continuum flux, C_i s are the peak constants, P_{ti} is the peak time value while R_{ti} and D_{ti} are the rise and decay times respectively of i th peak in the period considered for fitting. A total of 39 peaks were modeled and the distribution of the obtained rise and decay times is shown in Figure 2. The peaks were chosen such that the average of the five points with the current point at the center is the highest compared to immediate neighboring points. The distribution of both rise and decay times appears to be skewed towards the left with peaks around 2 days and some values extending up to 15 days. The rise and decay time distribution is shown in Figure 2.

3.2 Multi-wavelength variability

The variability in the light curve provides an indirect measurement of the size and location of the emission region where the broadband emission (light curves) are produced. The fast flux variability of the order of hours or minutes (Goyal et al. (2017), Goyal et al. (2018)) scales suggest a very small region very close to the supermassive black hole (SMBH). Many models have been proposed to explain that. The best-accepted model is the shock-in-jet (Marscher & Gear (1985)) model where the shock can be produced at the base of the jet with local fluctuations. Another possible explanation has been proposed recently known as magnetic-reconnection which happens at farther distances down the jet (Shukla & Mannheim (2020)). The location of the emission region is another long-standing problem in blazar physics. In some sources, It has been found that under the one-zone leptonic scenario the emission region is generally located within the boundary of the broad-line region (BLR). However, there have been many studies that show the location of the emission region can also be far down the jet outside the BLR.

The variability time scale can be estimated using the following expression,

$$F_2 = F_1 2^{(t_2 - t_1)/t_d} \quad (2)$$

where F_2 and F_1 are the fluxes measured at times t_2 and t_1 and the t_d is the flux doubling/halving time. The minimum variability times are calculated for the wavelengths shown in Figure 1 and the values are presented in Table 2. For the distribution of t_d values see Appendix A.

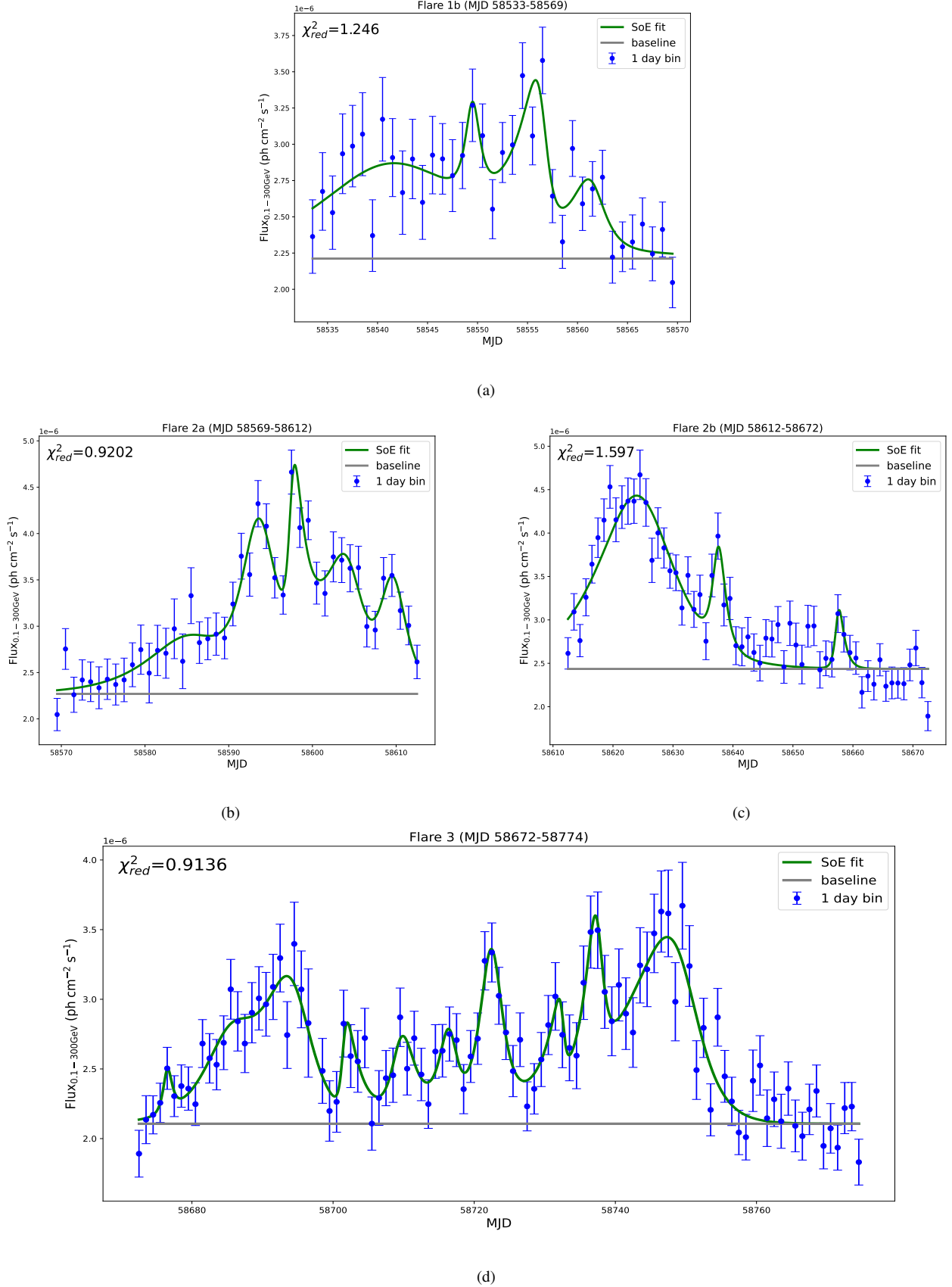
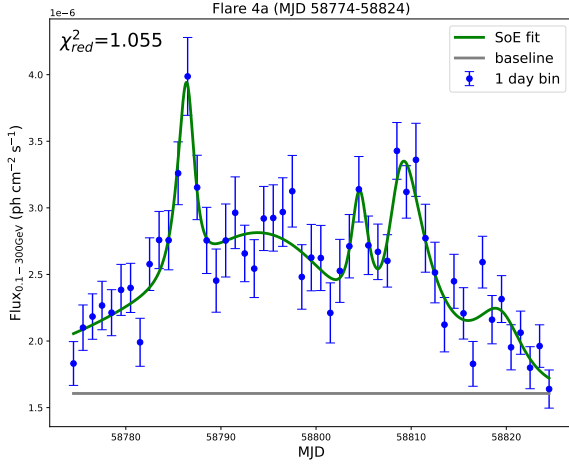
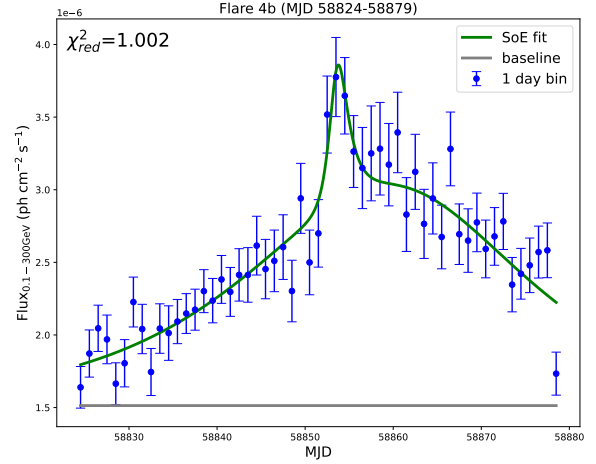


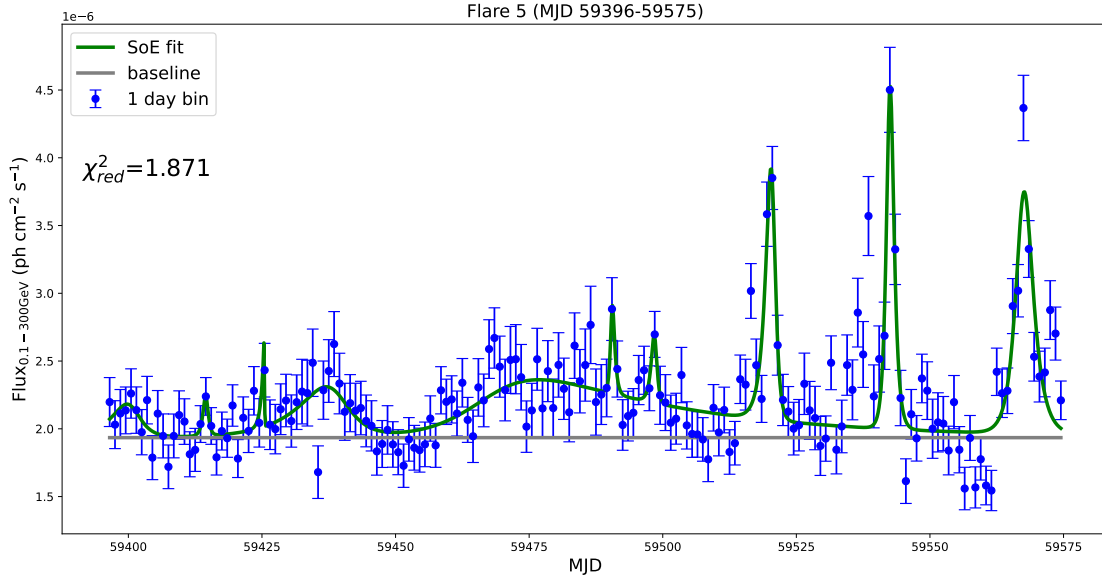
Figure 3. The local peaks in the γ -ray light curve for each flare are fitted with the Sum of Exponentials (SoE) function. The individual Flares 1, 2, and 4 are subdivided into two parts (a and b) favor of a better fit. A total of 39 peaks were modeled and the corresponding rise and decay times were estimated. The reduced χ^2 (χ^2_{red}) values are calculated to estimate the goodness-of-fit and are mentioned in each plot. Fitting for Flare 1a was not satisfactory due to data discontinuities and is excluded from the analysis.



(e)



(f)



(g)

Figure 3. (Continued)

4 GAMMA-RAY SPECTRUM

The γ -ray spectral analysis is done following the unbinned likelihood method. Analysis was performed using a user-contributed tool *likeSED3.py*⁵ with the NewMinuit algorithm for the flares 1-5. During the modeling, the parameters of sources outside the 10-degree ROI were kept constant while the ones inside 10 degrees were allowed to vary. The spectrum of the source (4FGL J0348.5-2749) was then divided into 28 bins in the 0.1-300 GeV energy range giving the same number of spectral points. The Power Law (PL), Log-Parabola (LP), Broken Power Law (BPL), and Power Law with Exponential Cut-off (PLExpCutoff) models (see equations 3-6) were used for fit-

ting these points. The parameters for each of the fits are given in Table 3 and the corresponding model plots are shown in Figure 4.

(i) Power Law (PL):

$$\frac{dN}{dE} = N_0 (E/E_0)^\gamma \quad (3)$$

(ii) Broken Power Law (BPL):

$$\frac{dN}{dE} = N_0 \times \begin{cases} (E/E_b)^{\gamma_1}, & \text{if } E < E_b \\ (E/E_b)^{\gamma_2}, & \text{otherwise} \end{cases} \quad (4)$$

(iii) Log-Parabola (LP):

$$\frac{dN}{dE} = N_0 \left(\frac{E}{E_b} \right)^{-(\alpha + \beta \log(E/E_b))} \quad (5)$$

⁵ <https://fermi.gsfc.nasa.gov/ssc/data/analysis/user/likeSED3.py>

Power Law							
Flare	$F_{0.1-300\text{GeV}}$ ($10^{-7} \text{ ph cm}^{-2} \text{ s}^{-1}$)	Prefactor (N_0) ($10^{-10} \text{ ph cm}^{-2} \text{ s}^{-1} \text{ MeV}^{-1}$)	Index (γ)	Scale (E_0) (MeV)		TS	TS_{curve}
1	9.513 ± 0.008	2.022 ± 0.001	-2.018 ± 0.0005			14525.93	-
2	11.085 ± 0.049	2.404 ± 0.009	-1.996 ± 0.003			25411.73	-
3	7.212 ± 0.046	1.501 ± 0.008	-2.040 ± 0.004	680.1		13420.26	-
4	6.189 ± 0.053	1.335 ± 0.009	-2.002 ± 0.006			11105.37	-
5	3.300 ± 0.067	0.714 ± 0.012	-2.001 ± 0.013			8909.44	-
Broken Power Law							
Flare	$F_{0.1-300\text{GeV}}$ ($10^{-7} \text{ ph cm}^{-2} \text{ s}^{-1}$)	Prefactor (N_0) ($10^{-10} \text{ ph cm}^{-2} \text{ s}^{-1} \text{ MeV}^{-1}$)	Index1 (γ_1)	Index2 (γ_2)	Break Value (E_b) (MeV)	TS	TS_{curve}
1	9.133 ± 0.022	0.3721 ± 0.0005	-1.924 ± 0.001	-2.234 ± 0.003	1692 ± 1.122	14447.65	-156.56
2	10.287 ± 0.024	1.345 ± 0.002	-1.821 ± 0.001	-2.207 ± 0.002	998.3 ± 0.671	23525.53	-3772.4
3	6.888 ± 0.036	1.352 ± 0.004	-1.894 ± 0.003	-2.181 ± 0.005	766.7 ± 1.143	13411.65	-17.22
4	5.564 ± 0.003	0.7686 ± 0.003	-1.781 ± 0.0003	-2.235 ± 0.0006	998.1 ± 0.1753	10659.25	-892.24
5	3.100 ± 0.085	0.390 ± 0.015	-1.844 ± 0.026	-2.189 ± 0.036	1005.0 ± 19.7	8931.38	43.88
Log-Parabola							
Flare	$F_{0.1-300\text{GeV}}$ ($10^{-7} \text{ ph cm}^{-2} \text{ s}^{-1}$)	Norm (N_0) ($10^{-10} \text{ ph cm}^{-2} \text{ s}^{-1} \text{ MeV}^{-1}$)	α	β	E_b (MeV)	TS	TS_{curve}
1	9.048 ± 0.056	2.185 ± 0.008	1.978 ± 0.003	0.5177 ± 0.0159		14461.04	-129.78
2	10.450 ± 0.103	2.673 ± 0.019	1.949 ± 0.006	0.709 ± 0.0333		23534.64	-3754.18
3	6.798 ± 0.014	1.647 ± 0.002	1.999 ± 0.001	0.6499 ± 0.0062	680.1	13386.68	-67.16
4	5.269 ± 0.004	1.486 ± 0.001	1.887 ± 0.001	-0.998 ± 0.002		10425.39	-1359.96
5	2.900 ± 0.027	0.789 ± 0.005	1.912 ± 0.006	0.836 ± 0.028		8560.39	-698.1
PLExpCutoff							
Flare	$F_{0.1-300\text{GeV}}$ ($10^{-7} \text{ ph cm}^{-2} \text{ s}^{-1}$)	Prefactor (N_0) ($10^{-10} \text{ ph cm}^{-2} \text{ s}^{-1} \text{ MeV}^{-1}$)	Index (γ)	Scale (E_0)	Cutoff (E_c) (10^4 MeV)	TS	TS_{curve}
1	9.211 ± 0.208	2.154 ± 0.042	-1.938 ± 0.018		2.992 ± 0.172	14486.28	-79.3
2	10.688 ± 0.002	2.665 ± 0.0004	-1.884 ± 0.0001		1.860 ± 0.002	25454.22	84.98
3	6.905 ± 0.010	1.629 ± 0.002	-1.937 ± 0.001	680.1	2.054 ± 0.020	13347.70	-145.12
4	5.843 ± 0.006	1.467 ± 0.001	-1.873 ± 0.001		1.806 ± 0.009	11010.50	-189.74
5	3.100 ± 0.006	0.800 ± 0.001	-1.852 ± 0.001		1.444 ± 0.001	8904.12	-10.64

Table 3. Spectral parameters of γ – ray SED fitted with four different models (Power Law, Broken Power Law, Log-Parabola, and PLExpCutoff). See Figure 4 for the model plots.

(iv) PLExpCutoff:

$$\frac{dN}{dE} = N_0 \left(\frac{E}{E_0} \right)^{\gamma_1} \exp(-E/E_c) \quad (6)$$

The Test Statistic (TS) value was chosen as a measure for the quality of the model fit and is computed from the likelihood values obtained from the modeling. The Test Statistic (TS) is given by $TS = -2 \ln (L_{\text{max},0}/L_{\text{max},1})$, where $L_{\text{max},0}$ is the maximum likelihood value without a source at a position, and $L_{\text{max},1}$ is the maximum likelihood value with a source. We have also examined the curvature in the spectrum by estimating the $TS_{\text{curve}} = 2 [\log \mathcal{L}(M) - \log \mathcal{L}(PL)]$, where \mathcal{L} is the likelihood function (Nolan et al. 2012) and M represents the model used for fitting which can be LP, BPL or PLExpCutoff. A larger negative value suggests a better fit. Considering that, we noted that for flares 1 and 2, BPL gave a better fit, and flares 3, 4, and 5 are represented best by LP. Similar results were also reported for other FSRQs in Britto et al. (2016) and Prince et al. (2017).

We also noticed that, in Table 3, for the Power Law case when the source goes from a low flux state to a high flux state the spectral index becomes softer and softer, suggesting a softer-when-brighter behavior. Previously in 2018, Angioni et al. (2019) observed a harder-

when-brighter trend during the large flaring state. This is a rare behavior seen in FSRQ. Most of the FSRQ show a harder-when-brighter behavior as can be seen in Abdo et al. (2010b); Britto et al. (2016) and Prince et al. (2017). However, softer-when-brighter behavior is more common in BL Lac-type sources. Although, the distinction is not much clear as discussed in Giommi et al. (2021).

5 MULTI-FREQUENCY SED MODELLING

The emission mechanisms of a blazar can be understood better from the modeling of broadband spectral energy distribution. We obtained the broadband SED using data from Fermi-LAT, Swift-XRT, and Swift-UVOT for each of the flare periods shown in Figure 1 except Flare 4 due to the lack of Swift data in that period. A typical broadband SED of a blazar has a two-hump structure with the lower energy hump associated with Synchrotron emission and the Inverse Compton scattered photons are assumed to be responsible for the higher energy hump. The seed photons for the IC scattering could be from inside the jet (i.e. synchrotron photon) or outside the jet from BLR or DT, and Accretion disk.

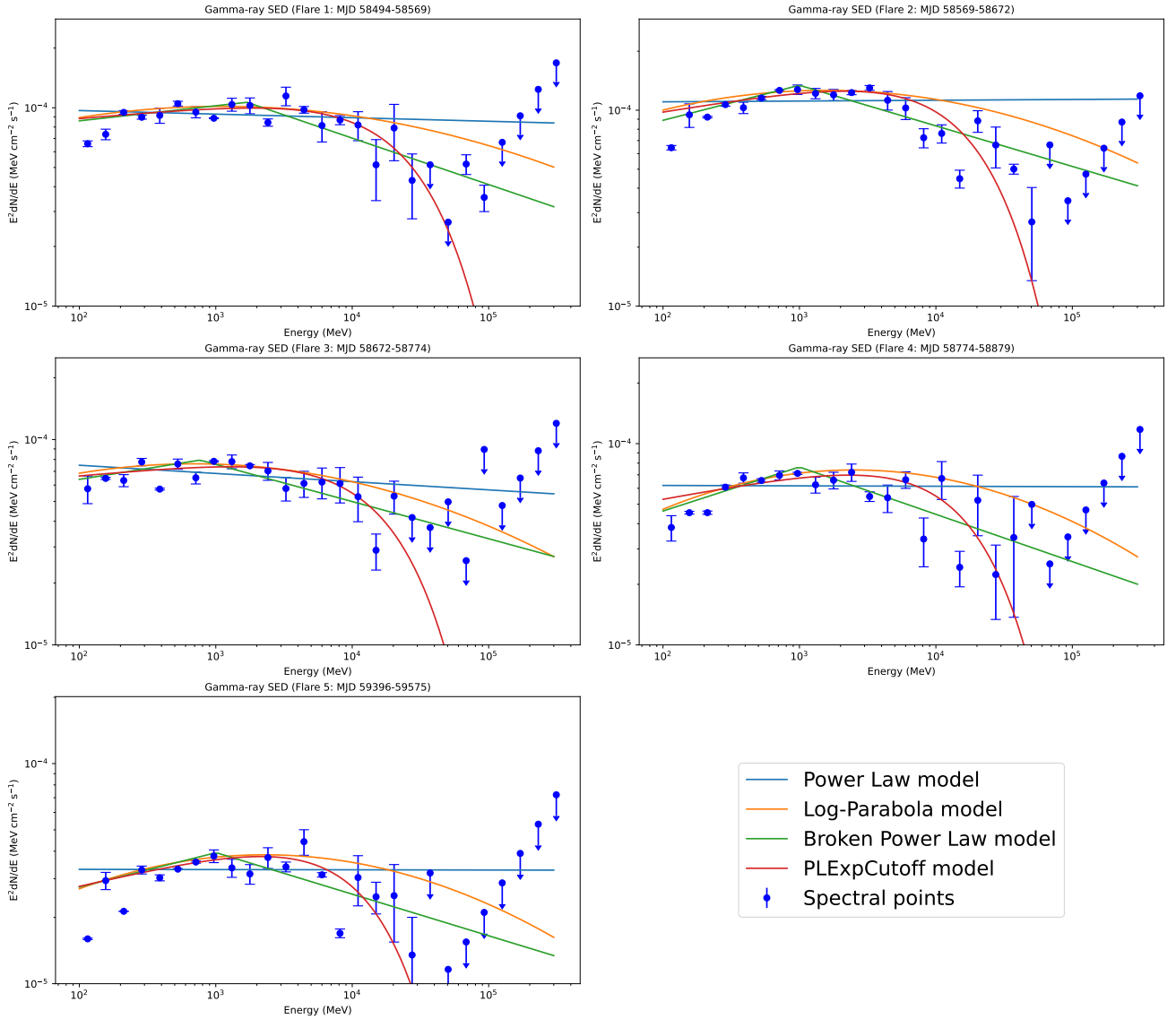


Figure 4. γ – ray SEDs obtained from Fermi-LAT data for each flare. The data is fitted with Power Law, Log-Parabola, Broken Power Law, and Power Law with Exponential Cutoff models. The 0.1-300 GeV energy range is divided into 28 bins using [likeSED.py](https://github.com/likeSED/likeSED.py) (a Fermi user-contributed tool) resulting in one spectral point for each bin. The five plots in this figure have common x and y axes. The results of the fit are given in Table 3.

We used JetSet⁶ (Tramacere (2020), Tramacere et al. (2011), Tramacere et al. (2009)) code for modelling the broadband SED. The Power Law with Cut-off (PLC) model was considered for the electron distribution with low energy spectral slope p . The non-thermal Synchrotron radiation is assumed to be responsible for the lower energy emissions i.e., the first hump in the SED. The higher energy photons are produced via the Synchrotron Self-Compton (SSC) and External Compton (EC) emission mechanisms. These two mechanisms are special cases of the Inverse Compton mechanism and are assumed to be responsible for the second hump. The seed photons for SSC emissions are the Synchrotron photons which are produced when electrons and positrons are accelerated in the strong magnetic field in the emission region near the central black hole. For EC emissions, the photon inputs are mainly sourced from (1) the direct emission

from the disk, (2) the reprocessed emission from BLR in the optical-UV frequency range, and (3) the reprocessed emission in the infrared region from the dusty torus. JetSet implements the modeling of BLR using the method in Donea & Protheroe (2003) and the disk emissions are modeled using chapter 5 of Frank et al. (2002) (for more detail see the description of JetSet).

The model considers a spherically symmetric region with a radius R' and electron density N as the emission region. It has a speed βc with respect to the observer, an entangled magnetic field B , and a bulk Lorentz factor $\Gamma = 1/\sqrt{1-\beta^2}$. The region moves at a small angle θ with the observer's line of sight and is located at a distance R_H from the central black hole. The corresponding Doppler factor is $\delta_D = 1/(\Gamma(1-\beta \cos \theta))$. In our case, we use $\Gamma = 60$ and take $\Gamma = \delta_D$ (Angioni et al. (2019)) which is quite high for an FSRQ type blazar (Hovatta et al. 2009; Wu et al. 2018). The synchrotron emission depends on the magnetic field and the speed of the relativistic electrons and is bounded by the Lorentz factors γ_{\min} and γ_{\max} .

⁶ <https://andreatramacere.github.io/jetsetdoc/html/index.html>

Symbol	Parameter [Units]	Flare 1	Flare 2	Flare 3	Flare 5
γ_{\min}	Low Energy Cut-Off [10^1]	1.77	5.42	3.45	9.45
γ_{\max}	High Energy Cut-Off [10^4]	1.62	3.11	1.96	5.81
N	Electron Density [$10^4/\text{cm}^3$]	14.36	4.43	5.76	9.46
γ_{cut}	Turn-Over Energy [10^3]	8.02	4.26	3.12	3.64
p	Low Energy Spectral Slope	2.16	2.09	2.22	2.14
R'	Emission Region Size [10^{15} cm]	1.00	1.00	1.00	0.37
R_H^*	Emission Region Position [10^{17} cm]	1.00	1.00	1.00	1.00
B	Magnetic Field [gauss]	0.56	0.77	0.92	1.27
δ_D^*	Doppler factor	60.00	60.00	60.00	60.00
z_{cosm}^*	Redshift	0.991	0.991	0.991	0.991
τ_{BLR}	Optical depth	0.07	0.07	0.07	0.07
$R_{\text{BLR}_{\text{in}}}^*$	Inner radius of BLR [10^{17} cm]	1.18	1.18	1.18	1.18
$R_{\text{BLR}_{\text{out}}}^*$	Outer radius of BLR [10^{18} cm]	1.18	1.18	1.18	1.18
L_{Disk}^*	Disk luminosity [10^{45} erg/s]	1.40	1.40	1.40	1.40
T_{Disk}	Disk temperature [10^5 K]	10.00	10.00	9.78	6.12
Energy Densities					
Symbol	Parameter [Units]	Flare 1	Flare 2	Flare 3	Flare 5
U'_{BLR}	BLR Energy Density [erg/cm 3]	14.86	14.86	14.86	14.86
U'_{Disk}	Disk Energy Density [erg/cm 3]	5.79	5.79	5.79	5.79
U'_e	Electron Energy Density [erg/cm 3]	8.77	7.17	5.28	22.38
U'_B	Magnetic Field Energy Density [10^{-2} erg/cm 3]	1.24	2.37	3.37	6.37
Jet Power					
Symbol	Parameter [Units]	Flare 1	Flare 2	Flare 3	Flare 5
P_{jet}	Total Jet Power [10^{45} ergs/s]	2.98	2.44	1.80	1.05
P_e	Jet Power in Electrons [10^{45} ergs/s]	2.97	2.43	1.79	1.05
P_B	Jet Power in Magnetic Field [10^{43} ergs/s]	0.42	0.80	1.14	0.30

Table 4. The parameters obtained from modeling the multi-frequency SEDs of Flares 1, 2, 3, and 5 using JetSeT. The Power Law with Cutoff (PLC) model was chosen for the radiating electrons. The energy densities and jet powers due to electrons and emission region magnetic field are subsequently computed. Additionally, the energy density of the Broad Line Region (BLR) and the accretion disk is computed in the rest frame of the emission region. In the top section, parameters with (*) are fixed during modeling.

The Broad Line Region (BLR) has inner and outer radii ($R_{\text{BLR}_{\text{in}}}$ & $R_{\text{BLR}_{\text{out}}}$) and an optical depth of τ_{BLR} . The primed quantities are in the comoving frame of the emission region. The emission region in the model is close to the disk and is assumed to be well inside the BLR (see Table 4) resulting in a relatively large contribution of Compton scattering from the accretion disk compared to the BLR and the dust torus. The accretion disk has a luminosity L_{Disk} and in a temperature T_{Disk} . The Synchrotron emission was restricted to the frequency range $10^{10} - 10^{18}$ Hz for effective fitting. Similarly, we constrained the Inverse Compton frequency range to $10^{21} - 10^{29}$ Hz. In the case of FSRQs, generally, EC is the dominant mechanism for γ -ray emission, as is evident for this source also. The seed photons for inverse Compton scattering are provided by the accretion disk as shown in Figure 5.

The energy densities in the accretion disk (U'_{Disk}) and the BLR (U'_{BLR}) are calculated directly by the model using JetSeT. The ratio $U'_{\text{Disk}}/U'_{\text{BLR}}$ is less than one for all the Flares (see Table 4). As expected the lower frequency emissions are dominated by Synchrotron and SSC components. The total power of the jet is estimated from the energy densities of leptons (U'_e), cold protons (U'_p), and magnetic field (U'_B) in the co-moving frame of the jet using the relation

$$P_{\text{jet}} = \pi R^2 c^2 \Gamma^2 (U'_e + U'_p + U'_B) \quad (7)$$

while the powers due to magnetic field (P_B) and leptons (P_e) are given by

$$P_B = \frac{1}{8} c R^2 \Gamma^2 B^2 \quad (8)$$

$$P_e = \frac{3c\Gamma^2}{4R} \int_{E_{\min}}^{E_{\max}} E \text{ PLC}(E) dE \quad (9)$$

where $\text{PLC}(E)$ is the Power Law with a Cutoff model as a function of energy and (E_{\min}, E_{\max}) represents the energy range of the leptons considered for modeling. The energy densities and powers differ by a factor $\pi R^2 c^2 \Gamma^2$ (see equation 7). For example, P_B and U'_B have the relation, $P_B = \pi R^2 c^2 \Gamma^2 U'_B$. The energy densities U'_e , U'_p , and U'_B are also estimated by the model and the contribution from U'_p is not included in this model. Consequently, the relation between the jet powers is $P_{\text{jet}} \approx P_e + P_B$. The respective values of parameters, energy densities, and jet power are mentioned in Table 4. The modeling was performed for different values of γ_{\min} and γ_{\max} and are adjusted for the best fit. The inner radius of the BLR region is set to 1.18×10^{17} cm using the scaling relation $R_{\text{BLR}} \sim (L_{\text{Disk}}/10^{45})^{1/2}$ cm (Ghisellini & Tavecchio (2009)) and $L_{\text{Disk}} = 1.4 \times 10^{45}$ erg/s (Angioni et al. (2019)). The L_{Disk} value is fixed in this model. $R_{\text{BLR}_{\text{out}}}$ is set to an order of magnitude higher than $R_{\text{BLR}_{\text{in}}}$ and R_H is set to the

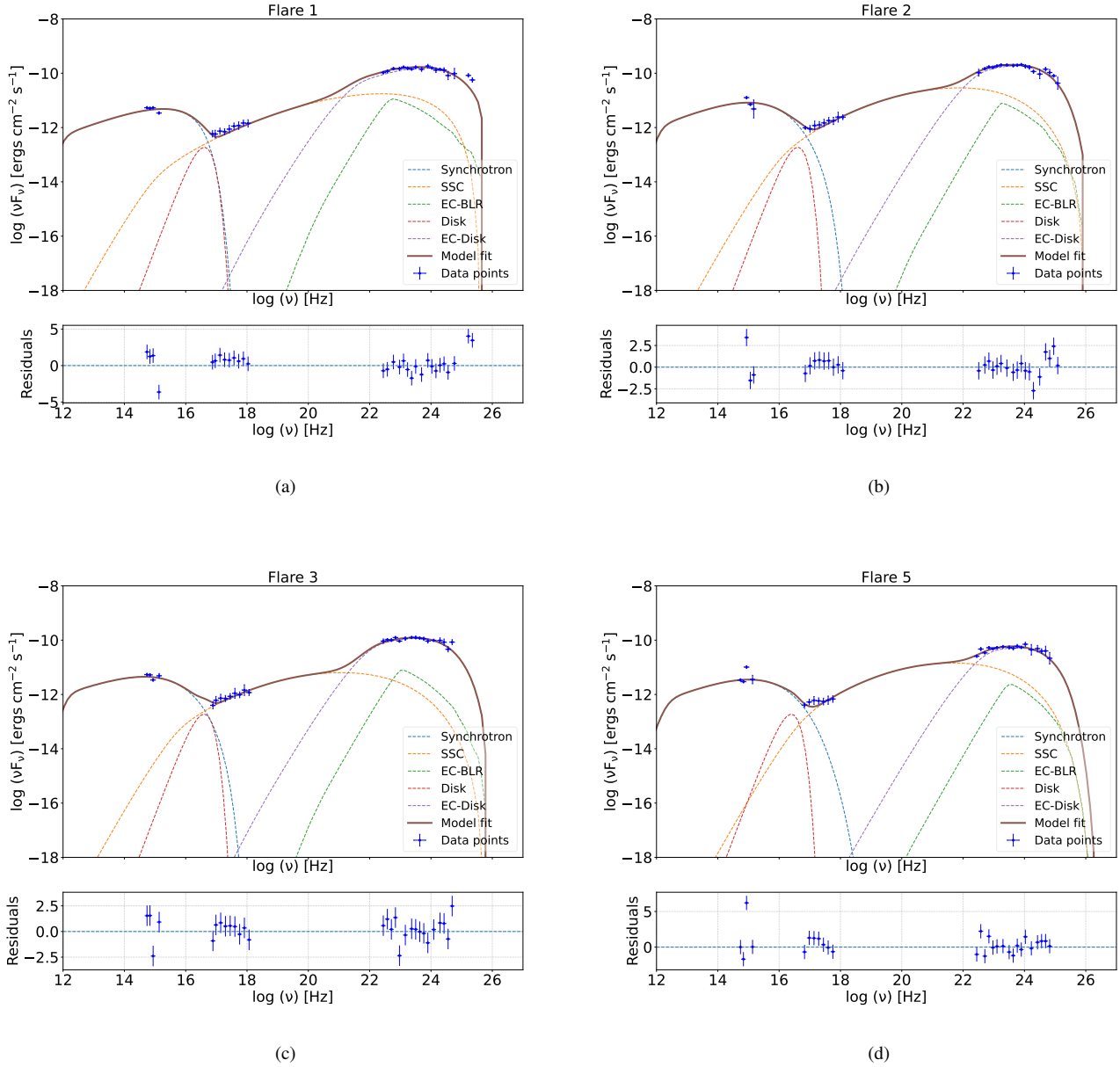


Figure 5. Multi-frequency SEDs obtained from Fermi-LAT, Swift-XRT, and Swift-UVOT for Flares 1, 2, 3, and 5 are modeled using *JetSeT*. The three clusters of data (from left to right) are from Swift-UVOT, Swift-XRT, and Fermi-LAT respectively.

default value in *JetSeT*. The P_{jet} value decreases with each flare but remains in the same order. The γ_{cut} value remains of the same order for the entire period of analysis indicating similar cut-off energy. In the low energy region, the spectral slope (p) fluctuates minimally in the 2.09–2.22 range which can be attributed to the stability of seed photon emissions. Swift-XRT and Swift-UVOT data for the period in Flare 4 are not available for broadband SED modeling.

The variability time scales from section 3.2 can also be used to estimate the size of the emission region using $R' \leq ct_{var}\delta_D/(1+z)$ (Abdo et al. (2011)). Using the minimum γ -ray variability ($t_{var} = 1.343$ days) we get a value of 1.05×10^{17} cm for R' and the corresponding values from the modeling are in the range $0.37 - 1.00 \times 10^{15}$ cm similar to the values in Angioni et al. (2019) where R' is described as the comoving radius of the blob. Performing

similar calculations using the values from Table 2, we find the values of R' to be in the range $0.08 - 2.53 \times 10^{17}$ cm in some cases an order of magnitude higher than the modeling results this could possibly happen due to lack of well-sampled data.

The distance of the emission region from the central black hole can be estimated from $R_H < c\Gamma^2 t_{var}/(1+z)$ (Abdo et al. (2011)). Taking $t_{var} = 1.343$ days (γ -ray minimum variability), the estimated upper limit of R_H value is 6.29×10^{18} cm and $R_H = 1.0 \times 10^{17}$ cm from the modelling. For the rest of the wavelengths in Table 2, the value range is $4.8 - 7.5 \times 10^{17}$ cm. Here we noticed that for though gamma-ray the location is not exactly matching with the modeling result but the value estimated with all other emissions is consistent with the modeling result. We believed that this could happen because of many free parameters in the SED modeling. During the modeling,

we noticed that the disk photon contributes more than the BLR photons and the gamma-ray is explained by EC-disk. This could be possible when the emission blob is too close to the central source. In our result, we see that the location of the blob is closer than the BLR location ($>10^{17}$) measured from the central source.

6 POWER SPECTRAL DENSITY

The variability in the source light curve can also be quantified by the power spectral density or PSD, which determines the amplitude of variation in the temporal light curve as a function of Fourier frequency or variability time scales (Ryan et al. 2019). PSD is important to understand the average properties of the variability, whereas the source light curve could be thought of as only a single realization of an underlying stochastic process as shown by Vaughan et al. (2003). We have derived the power spectral density or PSD using the discrete Fourier transformation (DFT). The shape of the PSD is best fitted with power law using the "power spectrum response" (PSRESP) method.

For an evenly sampled light curve $f(t_i)$ the RMS-normalized PSD is the squared modulus of the DFT. Assuming the light curve is sampled over time steps t_i and has a total number of points N , the RMS-normalized PSD can be defined as,

$$P(\nu_k) = \frac{2T}{\mu^2 N^2} \left\{ \left[\sum_{i=1}^N f(t_i) \cos(2\pi \nu_k t_i) \right]^2 + \left[\sum_{i=1}^N f(t_i) \sin(2\pi \nu_k t_i) \right]^2 \right\} \quad (10)$$

where μ is the mean of the light curve and $\nu_k = i/T$, $i = 1, 2, 3, \dots, N/2$ with the maximum frequency, Nyquist frequency, $\nu_{Nyq} = N/2T$.

The constant noise level is also estimated in form of normalized Poisson noise using the relation,

$$P_{Poisson} = \frac{\sigma_{err}^2}{\mu^2 (\nu_{Nyq} - \nu_{min})} \quad (11)$$

where σ_{err}^2 is the mean-variance of the measurement uncertainty.

Further, we have used the "Power Spectral Response (PSRESP)" method to tackle the distortions in PSD caused by the Fourier transform and estimate the best fit power law slope to the PSD. This method has already been used by many authors and is currently one of the best methods to describe the best fit PSD (Uttley et al. 2002; Chatterjee et al. 2008; Max-Moerbeck et al. 2014; Meyer et al. 2019; Bhattacharyya et al. 2020; Goyal et al. 2022). The detailed procedure of the PSRESP method can be seen in (Bhattacharyya et al. 2020; Goyal et al. 2022). In the PSRESP method, we choose the range of PSD slope starting from 0.5 to 3.0 with steps 0.05 and corresponding to each slope success fraction is defined (see Bhattacharyya et al. (2020) for more details on success fraction). The best fit PSD slope is determined as 2.15 ± 0.87 . As it has been seen that the blazar variability is a stochastic process and can be fitted with a single Power Law. The PSD slope, $\beta = 1$ corresponds to pink or flicker noise, and $\beta = 2$ represents the red noise. In our case, β covers the range 1.28–3.02 suggesting variability in the blazar is a stochastic process of correlated colored-noise type (Goyal 2020). The PSD can be used to find out the characteristic time-scale in the system and that can be used to constrain the size of the emission region. The characteristic time scale can be derived when the PSD deviates from the Power Law shape and show some kind of break in the power spectrum. Generally, the breaking time scale can be characterized as the time

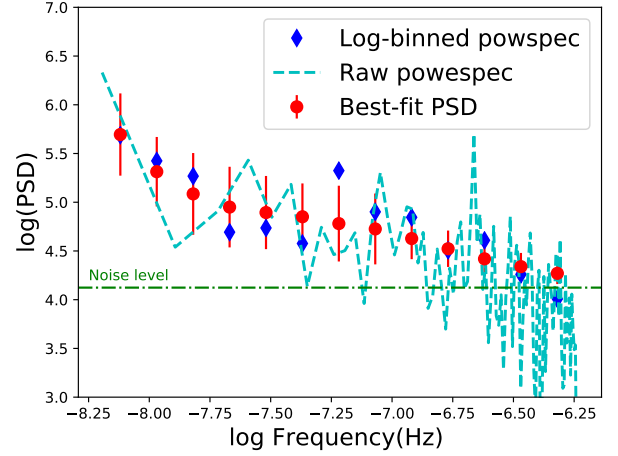


Figure 6. Best fit PSD for the gamma-ray light curve derived using the PSRESP method.

scale of variability in the source or the particle cooling or escape time scales (Kastendieck et al. 2011; Sobolewska et al. 2014; Finke & Becker 2014; Chen et al. 2016; Kushwaha et al. 2017; Chatterjee et al. 2018; Ryan et al. 2019; Bhattacharyya et al. 2020). It suggests that even longer data sets are required to see any break in the PSD and hence the characteristic time scale.

The PSD is derived for the long-term gamma-ray light curve and the resultant PSD is shown in Figure 6. The PSD can also be used to characterize the variability in other wavebands. The earlier results suggest that the variability in high energy bands (X-ray and gamma-ray) is characterized by pink or flicker noise (Abdo et al. 2010b; Isobe et al. 2014; Abdollahi et al. 2017) and in lower energy (radio and optical) by damped/red-noise type processes (Max-Moerbeck et al. 2014; Nilsson et al. 2018).

7 RESULTS AND DISCUSSION

In this paper, we analyzed the γ -ray flaring activity for the blazar PKS 0346-27 during the period 2019 January–2021 December (MJD 58484–59575). Most of the time during this slot this source was in a high state. We also analyzed the follow-up observations in X-ray and UV bands. The archival data of Swift X-ray, UVOT, and Fermi-gamma ray space telescope allowed us to investigate the multi-frequency SED of the source. We study the possible physical mechanism of the source and its jet parameters through theoretical modeling of the multiwavelength SED during four instances when the source was in a high state in γ -ray energies. A study of this source for an earlier period has been reported in Angioni et al. (2019).

We identify five flaring episodes for the γ -ray light curve. We fit each flare with Sum-of-Exponentials (SoE). The individual flares 1, 2 and 4 are again subdivided into two parts (a and b) for a better fit. The corresponding reduced χ^2 values have a range of 0.9–1.8. A total of 39 peaks were modeled and the corresponding rise and decay times were estimated. Our study shows the presence of fast variability during the brightest phase of flaring activity. We found that the fast rise and decays are more frequent which constrains the emission region to be very compact. The statistical distribution of the rise and decay times for the γ -ray light curve is shown in figure 2. We found all possible scenarios of symmetric and asymmetric peaks.

Considering the fact that the variability in the flare is caused by the interaction of the blob (emission region) with the standing shock (Blandford & Königl 1979; Marscher & Gear 1985). The symmetric flares are expected when the blob passes through the standing shocks and the particle radiates all its energy within the shock region within the light travel time ($\sim R/c$). Once the blob is moved out of the shock is moving we expect to see an asymmetric flare. This can also be seen as a scenario where the radiative cooling time is longer than the light travel time and as a result, a long-decay flare is observed. This means the radiative cooling time scale which includes synchrotron and IC cooling time scales is longer than the particle injection which is more or less instantaneous. Symmetric and Asymmetric flares are commonly seen in many blazars (Chatterjee et al. 2012).

We have estimated the fast variability time in all the emissions which constrains the size and location of the emission region down the jet. In X-ray, the fastest variability time is found to be 3.24 ± 0.26 days followed by γ -ray 1.34 ± 0.30 and optical-UV with an order of ~ 0.1 days. Taking the variability of γ -ray as a reference the size of the emission region is estimated as $\sim 1.05 \times 10^{17}$ cm. From the SED modeling, the best location of the emission region was found to be, $R_H = 1.0 \times 10^{17}$ cm which suggests the emission region is closer to the disk as the BLR starts from $> 10^{17}$ cm.

We obtained the γ -ray SEDs for each flare (figure 4). The γ -ray SEDs were fitted with Power Law, Log-Parabola, Broken Power Law, and Power Law with exponential cutoff models. The fitting parameters obtained from this study are shown in Table 3. In the γ -ray SED, we noticed a clear cut-off around 15-20 GeV (Table 3) and it could be due to $\gamma - \gamma$ absorption by the BLR photons (Liu & Bai 2006). Combining the information of fast variability and the location of the emission region, it is very much clear that the single-zone emission model would be the best choice to go ahead with. A single-zone leptonic emission model is a well-accepted and widely used scenario that has been used for many FSRQs type blazars (Angioni et al. 2019; Abdo et al. 2010d).

We model the multi-frequency SED of the source from γ -ray data of Fermi-LAT, X-ray data of Swift-XRT, and UV and optical data of Swift-UVOT for flares 1, 2, 3, and 5. The SED of all flares are well fitted with synchrotron, SSC, and EC from Disk and BLR. The EC-BLR appears to be sub-dominant compared to the EC-disk component. The direct disk thermal emission is also plotted along with the synchrotron and EC components in Figure 5. We have chosen a Power-law with a cutoff as particle distribution and a spherical blob of size, R' which is moving down the jet with Lorentz factor, Γ . The inner and outer radius of the BLR along with the location of the blob is fixed to a typical value during the modeling. The Doppler factor was also fixed at, $\delta_D = 60$ taken from Angioni et al. (2019). The parameters related to particle distribution such as minimum and maximum energy of the particles, cut-off energy, and power-law slope before cut-off, and the parameters related to the blob such as magnetic field and its size are kept free and optimized to the best value through the SED modeling. The BLR optical depth (τ_{BLR}) is another important parameter that is optimized to the best value for all the flares. The τ_{BLR} is found to be below 30% suggesting weak pair-production or $\gamma - \gamma$ absorption. We fixed the disk luminosity (L_{Disk}) and optimized the temperature for all four flares. From the L_{Disk} value, $R_{BLR_{in}}$ is estimated using a scaling relation mentioned in section 5.

A clear thermal signature from the accretion disk was also obtained in Angioni et al. (2019). The Broken Power Law was used for the electron distribution by Angioni et al. (2019) for the SED modeling while a Power Law with Cutoff is used in this analysis. The low energy spectral slope (p) has a range of 2.0-2.3 in 2019 and is similar to the

current model where the range is 2.09-2.22. The estimated magnetic field in the 2019 model has a range of 0.82-2.6 in the flaring state compared to the range of 0.56-1.27 in the current model. Both the models have similar order values for γ_{min} and γ_{max} . The power in each component was estimated and compared within the different states. Particles carry more power than magnetic fields suggesting a kinetic-dominated jet. Flare-1 carries the highest power followed by the other flares. The total jet power is estimated to be of the same order of magnitude over all the flares of the current model compared to values in the high state after flare A of Angioni et al. (2019) but are well within the Eddington luminosity of the source. The best fit disk temperature among the different flares is between $10^5 - 10^6$ K which is commonly seen in many FSRQs (Müller et al. 2018). The optimized value of the size of the emission region is found to be $\sim 10^{15}$ cm which is consistent with the observational upper limit estimate from the γ -ray variability time. One thing to note is the Angioni et al. (2019) studied only a small part of the flare between 2017-2019. However, the major flaring happened after that period which is presented in our work. As we know the blazars are highly variable and the flaring epochs of a source do not correlate with each other most of the time due to its stochastic nature therefore, it is less likely that we could derive the exact SED modeling parameters found in Angioni et al. (2019). In their work, they have fitted the gamma-ray part of the SED with the external Compton from the dusty torus, and sometimes the X-ray is well-fitted with SSC. They also noticed a shift in the synchrotron peak, as well as the EC peak towards higher frequency as the source, goes from a low state to a high flux state. In their case, in the low-state source behave as a low-synchrotron peaked (LSP) blazar and in the high state as an intermediate synchrotron peaked (ISP) blazar. They also suggest it could possibly be a "masquerading" BL Lac in its high state. However, in our study, we only modeled the flaring part so we do not notice any difference or shift in the synchrotron peak. In all cases, we have found that the synchrotron peak is in the range 10^{14-15} Hz as expected for ISPs, consistent with Angioni et al. (2019) at a high state. In our SED modeling, the X-ray is also well-fitted with SSC but for high-energy peaks, external Compton from the accretion disk was found to be the best scenario.

We have also produced the power spectral density for this source and a power law seems to produce the best fit with a slope of 2.15 ± 0.87 suggesting variability in this source is dominated by a stochastic process. Detailed γ -ray PSD of FSRQ and BL Lacs are studied in Abdo et al. (2010e) where they have found the power law as the best fit to their PSD without any break. The average PSD slope for a sample of FSRQ was derived as 1.4 ± 0.1 which is much harder than the PSD slope of individual source PKS 0346-27. The γ -ray PSD has also been done for many other blazars in past (Ackermann et al. 2010; Nakagawa & Mori 2013; Sobolewska et al. 2014; Ramakrishnan et al. 2015; Kushwaha et al. 2017; Goyal et al. 2022) and most of the time it is well fitted with single power-law. Nakagawa & Mori (2013) investigated the 15 AGN and found that 3C 454.3 show a characteristic time scale of 6.8×10^5 s and suggested an internal shock model for the variability. Similarly, Kushwaha et al. (2017) studied four Fermi-LAT sources including FRI radio galaxy NGC 1275, BL Lac Mrk 421, FSRQs B2 1520+31, and PKS 1510-089 and found a presence of a break which they argued that their results are broadly consistent with the statistical properties of the magnetic reconnection powered mini jets-in-a-jet model.

The hard γ -ray spectrum of PKS 0346-27 could make it a potential target for ground-based imaging atmospheric Cherenkov telescopes.

Recently, HESS has reported ⁷ to have detected this source with 5σ significance. Thus it is the highest redshift blazar surpassing the blazar S3 0218+35 ($z = 0.944$, Ahnen et al. (2016)) which is gravitationally lensed as well as surpassing the blazar PKS 1441+25 ($z = 0.940$, Ahnen et al. (2015)). FSRQs are difficult to detect during quiescent states, but because of the large flux variation during flaring states, they can be detected easily. CTA with an order of magnitude better sensitivity and with long exposure will be able to detect even during quiescent state at higher energies. That will provide an opportunity to compare emission mechanisms during the low and high states, as they are expected to be different. Therefore this source will be one interesting candidate for the southern array of the upcoming Cherenkov telescope array (CTA)⁸ (Bose et al. 2022). Future observations at VHE will be crucial for Extra-galactic Background Light (EBL) studies.

Fermi-LAT has been an important tool for observing high-energy blazars. In the future, it will play a crucial role in order to observe more high redshift ($z \geq 1$) blazars of the GeV energy range. Continued monitoring of the GeV sky will help to establish the duty cycles of γ -ray activities in relativistic jets. Moreover, Fermi-LAT is an invaluable tool in order to help ground-based γ -ray observatories such as Cherenkov telescopes to point their telescopes in the appropriate direction of the source. It will serve the same for the upcoming CTA. Therefore, continued observation of Fermi-LAT in the CTA era would be a great tool to better understand the physics of blazar jets, both in local and high redshift $z \geq 1$ universe.

ACKNOWLEDGEMENTS

We thank the anonymous referee for constructive comments and suggestions which have helped to improve the scientific merit of the work. S. Pramanick acknowledges the support of DST-INSPIRE Scholarship and Prime Minister's Research Fellowship (PMRF). R. Prince is grateful for the support of the Polish Funding Agency National Science Centre, project 2017/26/A/ST9/-00756 (MAESTRO 9) and MNiSW grant DIR/WK/2018/12 and European Research Council (ERC) under the European Union's Horizon 2020 research and innovation program (grant agreement No. [951549]). D. Bose acknowledges the support of Ramanujan Fellowship-SB/S2/RJN-038/2017. This work made use of Fermi telescope data and the Fermi tool package. This work also made use of publicly available packages JetSet and PSRESP. We used a Fermi-user-contributed tool `likeSED.py` for figure 4.

DATA AVAILABILITY

For this work, we have used data from Fermi-LAT, Swift-XRT, and Swift-UVOT telescopes. All the data are available in the public domain. Details are given in section 2.

REFERENCES

- Abdo A. A., et al., 2010a, *The Astrophysical Journal Supplement Series*, 188, 405
- Abdo A. A., et al., 2010b, *The Astrophysical Journal*, 710, 1271
- Abdo A., et al., 2010c, *The Astrophysical Journal*, 716, 30
- Abdo A. A., et al., 2010d, *The Astrophysical Journal*, 716, 30
- Abdo A. A., et al., 2010e, *The Astrophysical Journal*, 722, 520
- Abdo A. A., et al., 2011, *The Astrophysical Journal*, 733, L26
- Abdollahi S., et al., 2017, *The Astrophysical Journal*, 846, 34
- Abdollahi S., et al., 2020, *The Astrophysical Journal Supplement Series*, 247, 33
- Ackermann M., et al., 2010, *ApJ*, 721, 1383
- Aharonian F., et al., 2007, *The Astrophysical Journal*, 664, L71
- Ahnen M. L., et al., 2015, *The Astrophysical Journal Letters*, 815, L23
- Ahnen M. L., et al., 2016, *Astronomy & Astrophysics*, 595, A98
- Ajello M., et al., 2021, *The Astrophysical Journal Supplement Series*, 256, 12
- Angioni R., 2018, *The Astronomer's Telegram*, 11251, 1
- Angioni R., Nesci R., Finke J., Buson S., Ciprini S., 2019, *Astronomy & Astrophysics*, 627, A140
- Atwood W., et al., 2009, *The Astrophysical Journal*, 697, 1071
- Beasley A., Gordon D., Peck A., Petrov L., MacMillan D., Fomalont E., Ma C., 2002, *The Astrophysical Journal Supplement Series*, 141, 13
- Berton M., et al., 2018, *Astronomy & Astrophysics*, 614, A87
- Bhattacharyya S., Ghosh R., Chatterjee R., Das N., 2020, *The Astrophysical Journal*, 897, 25
- Blandford R. D., Königl A., 1979, *ApJ*, 232, 34
- Bolton J., Gardner F., Mackey M., 1964, *Australian Journal of Physics*, 17, 323
- Bose D., Chitnis V., Majumdar P., Acharya B. S., 2022, *The European Physical Journal Special Topics*, 231, 3
- Böttcher M., Reimer A., Sweeney K., Prakash A., 2013, *The Astrophysical Journal*, 768, 54
- Britto R. J., Bottacini E., Lott B., Razzaque S., Buson S., 2016, *ApJ*, 830, 162
- Carrasco L., Escobedo G., Recillas E., Porras A., Chavushyan V., Mayya D. Y., 2017, *The Astronomer's Telegram*, 10999, 1
- Chatterjee R., et al., 2008, *ApJ*, 689, 79
- Chatterjee R., et al., 2012, *ApJ*, 749, 191
- Chatterjee R., Roychowdhury A., Chandra S., Sinha A., 2018, *ApJ*, 859, L21
- Chen X., Pohl M., Böttcher M., Gao S., 2016, *MNRAS*, 458, 3260
- Dermer C., Schlickeiser R., Mastichiadis A., 1992, *Astronomy and Astrophysics*, 256, L27
- Donea A.-C., Protheroe R. J., 2003, *Astroparticle Physics*, 18, 377
- Finke J. D., Becker P. A., 2014, *ApJ*, 791, 21
- Frank J., King A., Raine D., 2002, *Accretion power in astrophysics*. Cambridge university press
- Ghisellini G., Tavecchio F., 2009, *Mon. Not. R. Astron. Soc.*, 397, 985
- Giommi P., et al., 2021, *MNRAS*, 507, 5690
- Goyal A., 2020, *Monthly Notices of the Royal Astronomical Society*, 494, 3432
- Goyal A., et al., 2017, *The Astrophysical Journal*, 837, 127
- Goyal A., et al., 2018, *The Astrophysical Journal*, 863, 175
- Goyal A., et al., 2022, *The Astrophysical Journal*, 927, 214
- Hovatta T., Valtaoja E., Tornikoski M., Lähteenmäki A., 2009, *A&A*, 494, 527
- Isobe N., et al., 2014, *The Astrophysical Journal*, 798, 27
- Kastendieck M. A., Ashley M. C. B., Horns D., 2011, *A&A*, 531, A123
- Kushwaha P., Sinha A., Misra R., Singh K. P., de Gouveia Dal Pino E. M., 2017, *ApJ*, 849, 138
- Liu H. T., Bai J. M., 2006, *ApJ*, 653, 1089
- Marscher A. P., Gear W. K., 1985, *ApJ*, 298, 114
- Massaro E., Giommi P., Leto C., Marchegiani P., Maselli A., Perri M., Piranomonte S., Sclavi S., 2009, *Astronomy & Astrophysics*, 495, 691
- Max-Moerbeck W., Richards J. L., Hovatta T., Pavlidou V., Pearson T. J., Readhead A. C. S., 2014, *Monthly Notices of the Royal Astronomical Society*, 445, 437
- Meyer M., Scargle J. D., Blandford R. D., 2019, *The Astrophysical Journal*, 877, 39
- Müller C., et al., 2018, *A&A*, 610, A1
- Nakagawa K., Mori M., 2013, *ApJ*, 773, 177
- Nesci R., 2018a, *The Astronomer's Telegram*, 11269, 1
- Nesci R., 2018b, *The Astronomer's Telegram*, 11455, 1

⁷ <https://www.astronomersteletgram.org/?read=15020/>

⁸ <https://www.cta-observatory.org/>

- Nilsson K., et al., 2018, *A&A*, **620**, A185
- Nolan P. L., et al., 2012, *ApJS*, **199**, 31
- Prince R., Majumdar P., Gupta N., 2017, *ApJ*, **844**, 62
- Raiteri C., et al., 2013, *Monthly Notices of the Royal Astronomical Society*, **436**, 1530
- Ramakrishnan V., Hovatta T., Nieppola E., Tornikoski M., Lähteenmäki A., Valtaoja E., 2015, *MNRAS*, **452**, 1280
- Ryan J. L., Siemiginowska A., Sobolewska M. A., Grindlay J., 2019, *ApJ*, **885**, 12
- Shukla A., Mannheim K., 2020, *Nature communications*, **11**, 1
- Sikora M., Begelman M. C., Rees M. J., 1994, *The Astrophysical Journal*, **421**, 153
- Sikora M., Stawarz Ł., Moderski R., Nalewajko K., Madejski G. M., 2009, *The Astrophysical Journal*, **704**, 38
- Sobolewska M. A., Siemiginowska A., Kelly B. C., Nalewajko K., 2014, *ApJ*, **786**, 143
- Thompson D., et al., 1993, *The astrophysical Journal supplement series*, **86**, 629
- Tramacere A., 2020, JetSeT: Numerical modeling and SED fitting tool for relativistic jets, Astrophysics Source Code Library, record ascl:2009.001 (ascl:2009.001)
- Tramacere A., Giommi P., Perri M., Verrecchia F., Tosti G., 2009, *A&A*, **501**, 879
- Tramacere A., Massaro E., Taylor A. M., 2011, *ApJ*, **739**, 66
- Urry C. M., Padovani P., 1995, *Publications of the Astronomical Society of the Pacific*, **107**, 803
- Uttley P., McHardy I. M., Papadakis I. E., 2002, *Monthly Notices of the Royal Astronomical Society*, **332**, 231
- Vallely P., et al., 2018, *The Astronomer’s Telegram*, **11337**, 1
- Vaughan S., Edelson R., Warwick R. S., Uttley P., 2003, *MNRAS*, **345**, 1271
- Voges W., et al., 1999, arXiv preprint astro-ph/9909315
- White G. L., Jauncey D. L., Savage A., Wright A. E., Batty M. J., Peterson B. A., Gulkis S., 1988, *The Astrophysical Journal*, **327**, 561
- Wu L., Wu Q., Yan D., Chen L., Fan X., 2018, *The Astrophysical Journal*, **852**, 45

APPENDIX A: MULTI-WAVELENGTH VARIABILITY PLOTS

This paper has been typeset from a \LaTeX file prepared by the author.

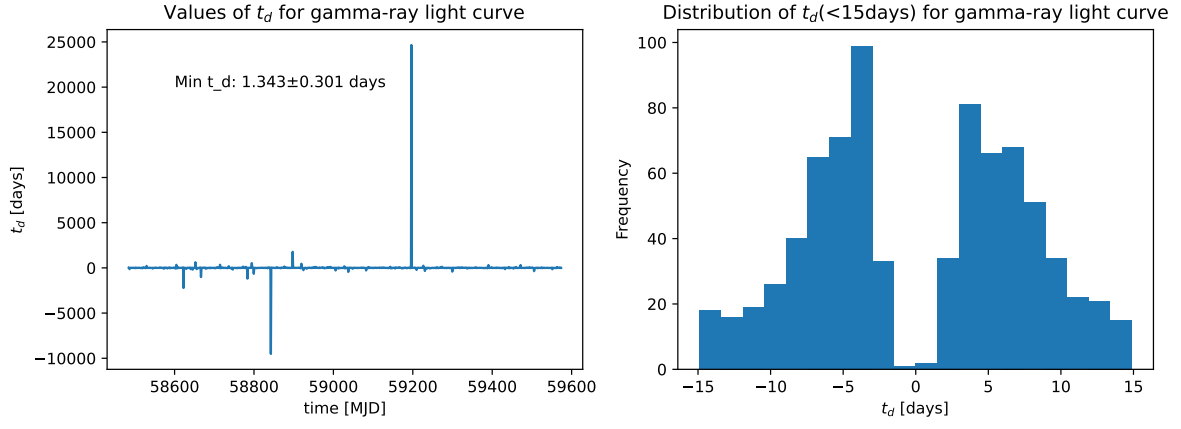


Figure A1. Variability time values and distribution for γ – ray light curve.

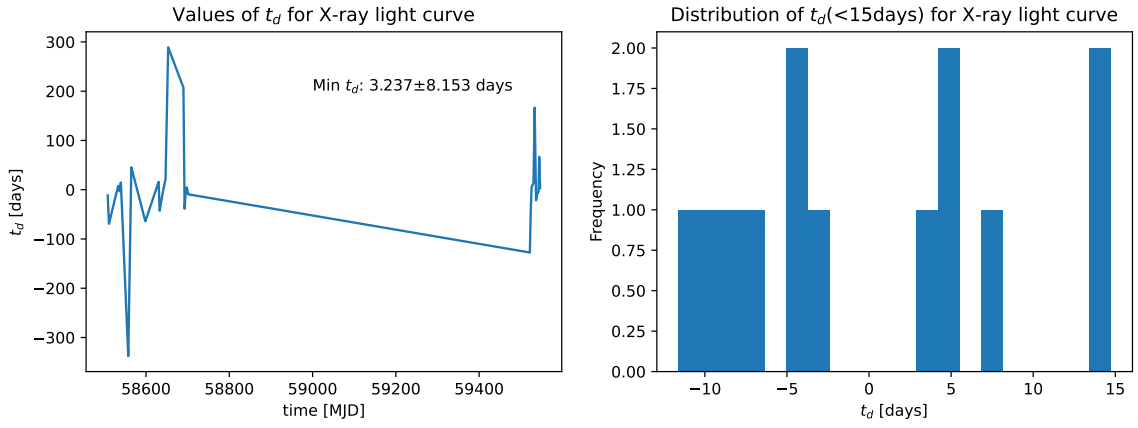
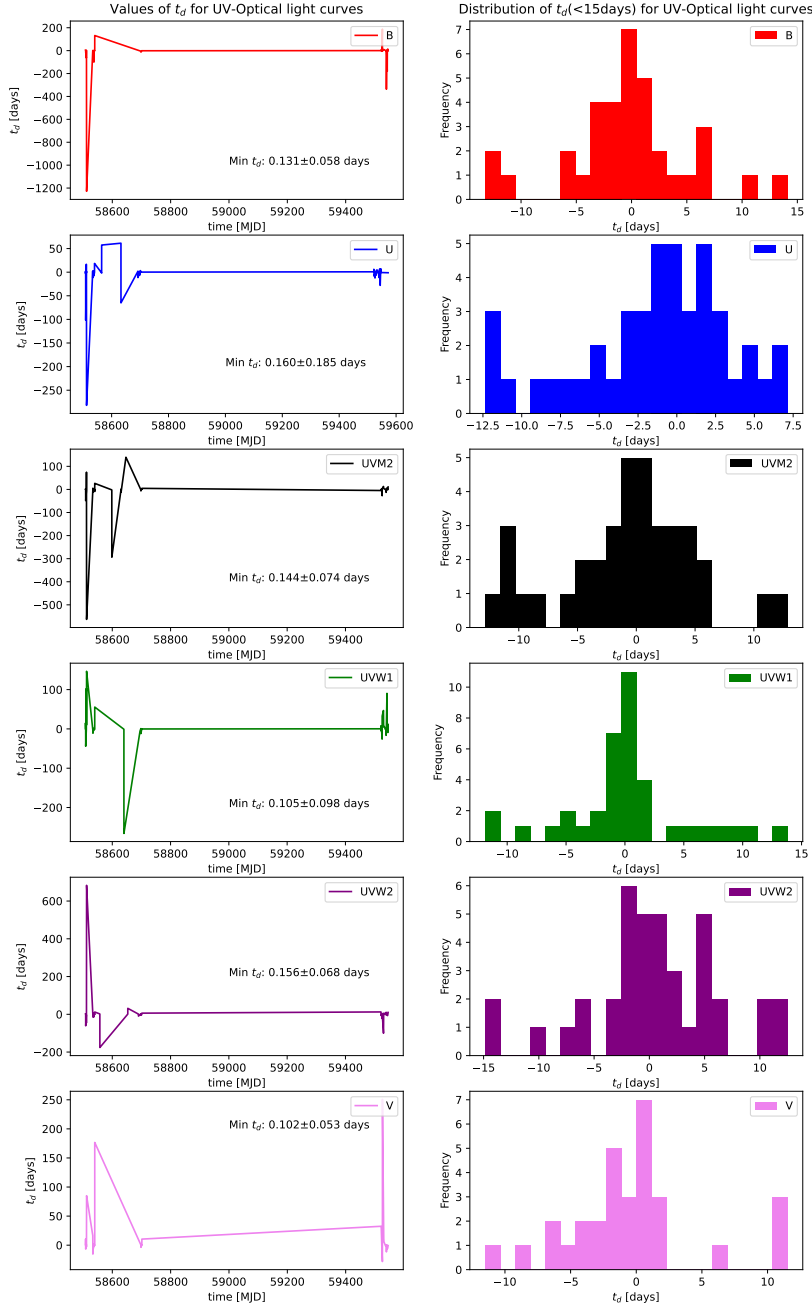


Figure A2. Variability time values and distribution for X-ray light curve.

**Figure A3.** Variability time values and distribution for UV and Optical light curves.